ACS APPLIED MATERIALS & INTERFACES

www.acsami.org

Research Article

Ion Current Rectification and Long-Range Interference in Conical Silicon Micropores

Mark Aarts, Willem Q. Boon, Blaise Cuénod, Marjolein Dijkstra, René van Roij, and Esther Alarcon-Llado*

Cite This: *ACS Appl. Mater. Interfaces* 2022, 14, 56226−56236

Read Online

ACCESS | Metrics & More | Article Recommendations | Supporting Information

ABSTRACT: Fluidic devices exhibiting ion current rectification (ICR), or ionic diodes, are of broad interest for applications including desalination, energy harvesting, and sensing, among others. For such applications a large conductance is desirable, which can be achieved by simultaneously using thin membranes and wide pores. In this paper we demonstrate ICR in micrometer sized conical channels in a thin silicon membrane with pore diameters comparable to the membrane thickness but both much larger than the electrolyte screening length. We show that for these pores the entrance resistance is key not only to Ohmic conductance around 0 V but also for understanding ICR, both of which we measure experimentally and capture within a single analytic theoretical framework. The only fit parameter in this theory is the membrane surface potential, for which we find that it is voltage dependent and its value is excessively large compared to the literature. From this we infer that surface charge outside the pore strongly contributes to the observed Ohmic conductance and rectification by a different extent. We experimentally verify this hypothesis in a small array of pores and find that ICR vanishes due to pore−pore interactions mediated through the membrane surface, while Ohmic conductance around 0 V remains unaffected. We find that the pore−pore interaction for ICR is set by a long-ranged decay of the concentration which explains the surprising finding that the ICR vanishes for even a sparsely populated array with a pore−pore spacing as large as 7 μm.

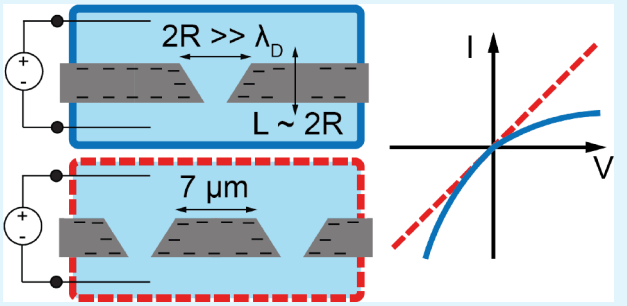

KEYWORDS: *conical micropore, ion current rectification, thin membrane, pore array, pore−pore interaction, electro-osmosis, Poisson−Nernst−Planck−Stokes equation*

INTRODUCTION

Ionic transport near solid−liquid interfaces can differ drastically from that in bulk due to Coulombic interactions with the surface.[1] Such interface effects can be used to tailor nanofluidic devices,[2] finding applications in desalination,[3,4] ionic circuitry,[5,6] biochemical sensing,[7−11] energy harvesting,[12,13] and neuromorphic signaling.[14−16] A particularly useful element for directional control of ionic currents is a current rectifier,[9,17−19] also known as a diode. In fact, the phenomenon of ion current rectification (ICR) has been observed and extensively studied in nanochannels.[20−23]

The ICR originates from an asymmetry in the ionic current along the length of the channel due to a varying relative contribution to the ionic current of the charge-selective electric double layer (EDL) that screens the charge on the channel walls. Typically, ICR is demonstrated in nanoscale conical channels, where EDL overlap occurs on the narrow end of the channel.[21,22] In general, the ICR mechanism for a geometrically asymmetric, or tapered, channel can be understood by considering that the relative contribution of the salt current through the EDL to the total current is smaller at the wide opening than at the narrow opening.[24,25] This results in an asymmetry of the transference (i.e., the partial current due to either ionic species). Considering a channel with a negative surface charge on its wall, resulting in an EDL with excess positive ionic charge, an electric field directed toward the narrow end leads to more ions leaving the small opening than entering the large opening (before steady state is reached), resulting in depletion of ions inside the channel and a suppressed conductance.[26] The opposite is true for an oppositely directed electric field, resulting in accumulation of charge carriers and enhanced conductance. More broadly, the required asymmetry in transference can be introduced not only by geometry but also by a variation of e.g. charge or concentration.[24,26,27]

For application purposes regarding larger scale porous membranes, a low electric resistance of the channel is desirable

Received: June 28, 2022
Accepted: November 28, 2022
Published: December 9, 2022

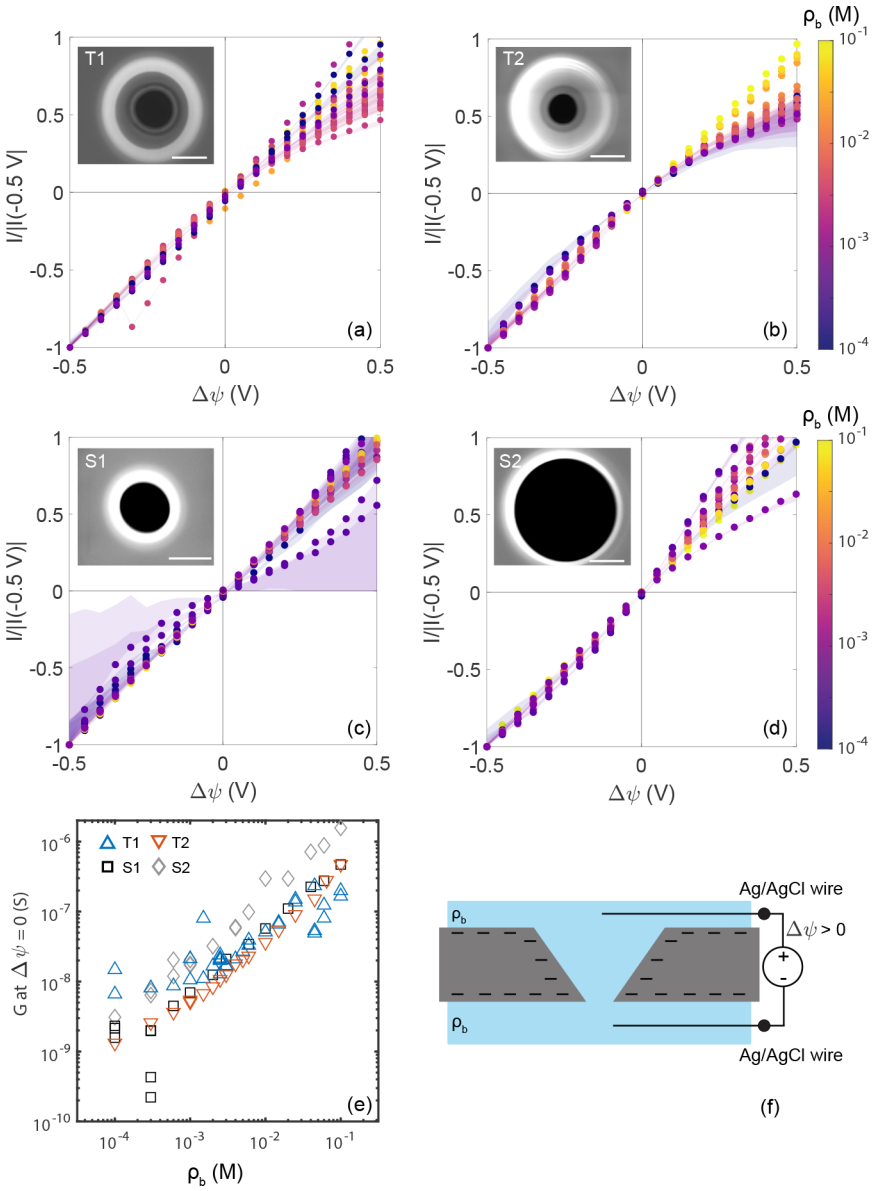

Figure 1. (a–d) Experimental current–voltage (I–V) curves, normalized at a potential drop of −0.5 V at various KCl concentrations $\rho_b \in \{10^{-4}–10^{-1}\}$ M indicated by the color scale. The shaded region indicates uncertainty in the measurement due to the leakage current obtained from an as-received membrane (SI-3). Systematic current rectification is observed for tapered pores T1 and T2 with the conductivity at +0.5 V being lower than at −0.5 V. The inset shows scanning electron microscopy images of the tapered pores T1 (a) and T2 (b) and straight pores S1 (c) and S2 (d) after fabrication. The scale bars are 1 μm. (e) Conductance of the pores at 0 V as a function of KCl concentration $\rho_b(M)$. (f) Schematic of the experimental setup where 2 aqueous reservoirs of equal KCl concentration are separated by the membrane with a single pore. The polarity of the potential is such that positive potentials indicate the anode being in the reservoir facing the large opening of the pore.

to mitigate Ohmic losses. Two intuitive ways to construct a channel with low resistance are by making (i) larger openings[26] or (ii) shorter channels.[28,29] Considering the accumulation/depletion mechanism described above, recent theoretical work predicts that ICR can also occur in wide channels without overlapping electric double layers, as long as a substantial part of the ionic current is due to surface conductance.[26,30–34] In fact, ICR in mesoscopic channels[35] and chemically modified micrometer-sized systems have recently been observed.[32,36,37] For thin membranes with short channels, on the other hand, it has become clear that the applied potential partially drops outside the channel rather than fully over the channel itself.[29,38–41] These extended entrance effects give rise to an edge, or access, resistance and become relevant for the behavior of a fluidic pore with a channel length of the order of the diameter, which can either positively contribute to ICR or interfere destructively in arrays of pores.[41–43] As of now however, such pore–pore interactions are still poorly understood.

In this work we fabricate conical, i.e., geometrically asymmetric, fluidic micropores in thin (2 μm) crystalline silicon membranes, with base and tip radii of $R_b \approx 1.5$ μm and $R_t \approx 0.5$ μm, respectively, such that even the smallest of these channel dimensions is larger than the typical electrolyte screening length by more than an order of magnitude. We demonstrate that these pores exhibit ion current rectification, and we develop an analytical theory for the channel conductance in which the surface potential is the only fit

https://doi.org/10.1021/acsami.2c11467
ACS Appl. Mater. Interfaces 2022, 14, 56226–56236

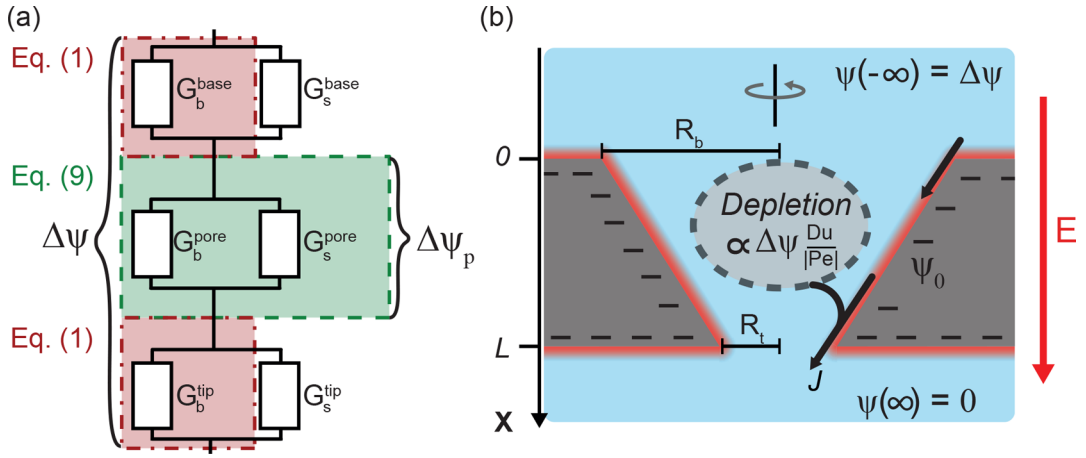

Figure 2. (a) Schematic equivalent circuit of a pore featuring bulk and surface conductance G_b^i and G_s^i, respectively, at the base, at the tip, and within the pore region. The elements considered in our analytical model are highlighted, where part of the applied potential $\Delta\psi$ drops over the edge resistance (red dash-dotted region), as captured by eq 1. The conductance of the pore with the remaining potential $\Delta\psi_p$ (green dashed region) is described by eq 9. (b) Representation of the conical system under consideration with base and tip radii R_b and R_t, respectively, and an electric field $-\partial_x\psi = E$ pointed toward the tip. As outlined in the text, the depletion of ions in the channel is proportional to the potential drop $\Delta\psi$ times the ratio of the Dukhin (Du) and Péclet (Pe) numbers as shown in eq 8a and illustrated here for a channel wall with a negative surface charge resulting in depletion for a positive potential drop due to a salt flux J (black arrow) through the electric double layer (EDL) that increases toward the tip.

parameter. We stress that the (Ohmic) channel conductance at low applied potentials and ICR are distinct phenomena, and we find that we need a different surface potential to fit the experimental data to these two effects, with both surface potentials being very large, implying a very large surface charge. We interpret the value of these fitted surface potentials as nonphysical and rather attribute this excessively large charge to a contribution of conduction along the planar membrane surface outside the channel at the inlet and outlet of the pore unaccounted for in our model. By connecting this required surface charge to an effective area, we estimate that this membrane surface conduction is relevant up to distances around the pore opening as large as 7.4 μm for Ohmic channel conductance and 15.0 μm for ICR, implying that a larger area around the pore is required for ICR. We test this hypothesis by fabricating a small array of pores with a 10 μm spacing ($\approx 10^6$ pores/cm^2). Indeed, we find that at this low pore density the Ohmic conductance remains unaffected but that the ICR vanishes for the array. Extended entrance effects at the micrometer scale therefore appear to play a significant role in the required asymmetry in ion transport through pores in thin membranes, which we attribute to the long-ranged decay of the electric field outside the pore. This electric field creates a concentration profile with a similar long-ranged, inverse square with distance, decay into the bulk. This scale-free decay introduces long-ranged pore−pore interactions for thin pores, which become particularly relevant in array configurations typical for membranes.

EXPERIMENTAL SECTION

For our conductance measurements we fabricate single micrometer sized pores, which are either straight or tapered, in 2 ± 0.5 μm thick crystalline silicon membranes using a focused ion beam (FIB). Si is a reliable and cross-compatible platform that allows for precise pore manufacturing. The taper is created by writing concentric circles with decreasing radius, resulting in an asymmetric pore, as verified by atomic force microscopy in SI-1. Conductance measurements are performed by placing the membrane between two aqueous reservoirs containing KCl of equal bulk concentration (ρ_b) and applying a potential between the reservoirs using Ag/AgCl wire electrodes (Figure 1f and SI-2). Of note is the polarity of the applied potential, where positive potentials indicate the anode being in the reservoir facing the large opening of the pore.

We record quasi-static current−voltage (I−V) curves between −0.5 and 0.5 V (see the Methods section) at different reservoir KCl bulk concentrations ρ_b ranging from 10^{-1} to 10^{-4} M for 4 membranes containing a single pore. The insets of Figure 1a−d show scanning electron microscopy (SEM) images directly after fabrication of the tapered pores T1 (base and tip radii $R_b \simeq 1.5$ μm, $R_t \simeq 0.5$ μm) and T2 ($R_b \simeq 1.5$ μm, $R_t \simeq 0.4$ μm) and two straight reference pores S1 ($R_b = R_t \simeq 0.6$ μm) and S2 ($R_b = R_t \simeq 1.5$ μm).

The corresponding I−V curves are shown as circles in Figure 1a−d, where the colors label the salt concentration ρ_b. As the magnitude of the current response varies by several orders of magnitude over the salt concentration range, the current is normalized to the value at an applied potential of −0.5 V for visibility. The shaded regions indicate the possible contribution from leakage current through the membrane, averaged from measurements on an as-received membrane without a pore (SI-3). Because of the range in magnitude of the measured currents, this is most relevant for the lowest concentrations and the smallest pore (S1). The conductance at 0 V as a function of concentration is shown in Figure 1e. A linear decrease of the conductance with decreasing concentration is observed with the conductance saturating at $\rho_b < 1$ mM.

At the highest concentrations (yellow, $\rho_b = 0.1$ M), and therefore the smallest Debye length ($\lambda_D \simeq 1$ nm), all pores show a linear I−V response, consistent with bulk dominated transport. At lower concentrations, however, conductance through the tapered channels starts to show ion current rectification. It should be noted that even at the lowest concentration, $\rho_b = 0.1$ mM, the electrolyte screening length $\lambda_D \simeq 30$ nm is much shorter than the smallest tip radius, so that the micropores are well outside the regime of EDL overlap. While some curves for the straight pores S1 and S2 show an erratic deviation from ideal symmetrical conductance, the tapered pores T1 and T2 show systematic rectification, where the conductance at positive potentials is smaller than that at negative potentials.

Theoretical Framework. In the following, we present a model for the potential-dependent conductance of a tapered pore and obtain a closed-form expression that simultaneously describes Ohmic conductance and ion current rectification. Currently in the literature there are two, complementary, theories for current rectification without EDL overlap for pores with large aspect ratio. The theory by Cengio[30]

https://doi.org/10.1021/acsami.2c11467
ACS Appl. Mater. Interfaces 2022, 14, 56226−56236

and Poggioli[26] describes ICR through the variation of the surface conductance over the pore length but neglects electro-osmotic flow, while the theory of ref 25 (developed by some of the present authors) does account for this flow but fails at extremely low salt concentrations. Hence both theories are complementary rather than mutually exclusive: refs 26 and 30 are valid at all concentrations, while the theory of ref 25 is valid at all flow rates. We will find that our experiments show characteristic flow-sensitive behavior, and therefore we build on the theory of ref 25. However, to describe our experiments, either theory would need to be extended as the membranes thickness here is similar to the radius of the pores, and the theory therefore has to account for the electric edge resistance which is comparable to the pore resistance. There is a variety of theories available in the literature accounting for Ohmic edge resistance,[2,29,38−40,44] the most commonly used one by Hall,[39] which we reproduce here. In this work we will find that edge resistances do not only alter Ohmic conductance but also significantly alter rectification. In the following section we extend the theory of ref 25 to account for edge effects.

The introduction of non-negligible edge resistances implies an equivalent electric circuit as illustrated in Figure 2a, which considers not only bulk and surface contributions to the conductance inside the pore (G_b^{pore} and G_s^{pore}) in parallel[45,46] but also two base (G_b^{base} and G_s^{base}) and tip (G_b^{tip} and G_s^{tip}) conductances. Only recently has it been shown that the charged surface outside of the membrane contributes to edge resistance,[2,38] but unfortunately our model is not able to explicitly account for the base and tip surface conductances (G_s^{base} and G_s^{tip}, respectively) even though we will see these charged regions do contribute significantly to both experimental Ohmic conductance and ICR. Instead, we implicitly account for the charge on the outside membrane through an "apparent" (large) surface charge within the pore, inflating the pore surface conductance G_s^{pore} and total conductance G. Hence, our large "apparent" surface charge will account for outer-membrane conductance increasing the well-known bulk edge conductances as described by Hall.[39] These parallel edge surface and bulk conductances are in series with the pore resistances as depicted in Figure 2a, which for the present system parameters ensures that the potential drop over the pore $\Delta\psi_p$ is significantly smaller than the total bias $\Delta\psi$. This decreased potential drop does not only reduce the current through the pore but also lowers the electro-osmotic flow and concentration polarization within the pore. To obtain $\Delta\psi_p$ we consider, in cylindrical (x,r,θ) coordinates, two bulk reservoirs in the half spaces $x < 0$ and $x > L$ connected by an azimuthally symmetric conical channel of length L as depicted in Figure 2b with base radius R_b at the inlet ($x = 0$) and tip radius R_t at the outlet ($x = L$), such that the radius of the channel reads $R(x) = R_b - (x/L)(R_b - R_t)$ for $x \in \{0, L\}$. The potential drop over the inside of the pore can be calculated using two assumptions: (i) that the electric field at the tip (and base) decays as a monopole $-\nabla\psi \propto 1/(r^2 + x^2)$ into the bulk far from the pore (as noted by ref 41) and (ii) that the electric field within the pore is divergence-free, such that electroneutrality is obeyed. From these assumptions it follows that the pore-potential drop $\Delta\psi_p = -\int_0^L \partial_x\psi \, dx$ is given by

$$\Delta\psi_p = \frac{\Delta\psi}{1 + \frac{\pi}{4L}(R_b + R_t)} \tag{1}$$

which we derive and verify in SI-4. We note that the edge resistance is negligible in the long-channel limit $L/R_b \gg 1$, as eq 1 reduces to $\Delta\psi_p \simeq \Delta\psi$ in this limit. In the geometry of our experiments the reduced potential $\Delta\psi_p$ given by eq 1 does not only effectively halve the electric current (as $L \approx R_b + R_t$ for our experimental geometries), but as noted it will also significantly influence current rectification. As eq 1 accounts for the influence of bulk-edge resistance (red regions in Figure 2a) for both the electric current and (electro-osmotic) flow and we use an effective surface charge σ as proxy for the surface-edge resistance, from now on our mathematical analysis will pertain only to the inner-pore region (green-shaded region in Figure 2a) therewith following ref 25.

The electric potential difference over the pore $\Delta\psi_p$ does drive not only ion fluxes $\mathbf{j}_\pm(x,r)$ of the cations (+) and anions (−) but also a fluid flow with a velocity field $\mathbf{u}(x,r)$. The salt flux $\mathbf{j}_s = \mathbf{j}_+ + \mathbf{j}_-$ and electro-osmotic flow $\mathbf{u}$ will be key to understanding the electric current $\mathbf{j}_e = \mathbf{j}_+ - \mathbf{j}_-$. The resulting salt concentration $\rho_s(x,r) = \rho_+(x,r) + \rho_-(x,r)$ due to the inhomogeneous salt current is of key importance for current rectification, while the space-charge $e\rho_e(x,r) = e(\rho_+(x,r) - \rho_-(x,r))$ outside the electric double layer is of secondary importance as was shown in ref 25. The ionic fluxes and concentrations satisfy the Nernst−Planck eqs 2 and 3 which describe diffusion, conduction, and advection, while the electric potential satisfies the Poisson eq 4 in terms of the electric space charge density $e\rho_e$. The fluid flow in the low-Reynolds number regime of interest here is given by the Stokes eq 5 which includes an electric body force $-e\rho_e\nabla\psi$, and the steady-state condition of interest leads to the condition of divergence-free fluxes (eq 6), which all accumulates into

$$\mathbf{j}_e = -D\left(\nabla\rho_e + \rho_s\frac{e\nabla\psi}{k_BT}\right) + \mathbf{u}\rho_e \tag{2}$$

$$\mathbf{j}_s = -D\left(\nabla\rho_s + \rho_e\frac{e\nabla\psi}{k_BT}\right) + \mathbf{u}\rho_s \tag{3}$$

$$\nabla^2\psi = -\frac{e}{\varepsilon}\rho_e \tag{4}$$

$$\eta\nabla^2\mathbf{u} - \nabla P - e\rho_e\nabla\psi = 0 \tag{5}$$

$$\nabla\cdot\mathbf{j}_\pm = 0, \quad \nabla\cdot\mathbf{u} = 0 \tag{6}$$

Here eq 2 shows explicitly that the salt concentration $\rho_s = \rho_+ + \rho_-$ determines the electric conductivity of the charge current $\mathbf{j}_e$. To obtain the pore conductance, we consider both reservoirs with a dilute (monovalent) KCl solution of concentration ρ_b, viscosity $\eta = 1$ mPa s, a dielectric permittivity $\varepsilon = 80\varepsilon_0$, with ε_0 the permittivity of vacuum, and a fixed temperature $T = 298$ K, which is constant throughout the system. Deep into the bulk of the base-connected reservoir, $x \ll -L$, we impose that the K^+ and Cl^- concentrations $\rho_\pm = \rho_b$, $P = P_0$, and $\psi = \Delta\psi$, and deep into the tip-connected reservoir, $x \gg 2L$, we impose $\rho_\pm = \rho_b$, $P = P_0$, and $\psi = 0$. Here the reference pressure $P_0 = 1$ atm. For K^+ and Cl^- we use equal diffusion coefficients $D = 1$ nm^2 ns^{-1}, which is somewhat smaller than the bulk diffusion constant at 20 °C and 0.1 M.[47,48] Such a discrepancy between channel and bulk diffusion constants has been noted in ref 40.

In thermodynamic equilibrium with vanishing potential drop between the reservoirs ($\Delta\psi = 0$) and vanishing fluxes, the PNPS eqs 2−6 reduce to Poisson−Boltzmann theory which describes a diffuse layer of net ionic charge near the surface, known as the electric double layer (EDL) with typical thickness $\lambda_D = (8\pi\lambda_B\rho_b)^{-1/2}$ and Bjerrum length $\lambda_B = e^2/(4\pi\varepsilon k_BT) \simeq 0.7$ nm. Outside this layer all concentrations $\rho_\pm(x,r)$ are equal to ρ_b and there is no electric field, $-\nabla\psi(x,r) \simeq 0$. In equilibrium the surface charge density $e\sigma$ obeys the Gouy−Chapman equation, $2\pi\lambda_B\lambda_D\sigma = \sinh(e\psi_0/2k_BT)$.[49] Here ψ_0 is the surface potential of the channel wall, which we will use as a fit parameter below, taken to be constant between all geometries and at all concentrations thereby implicitly accounting for a concentration-dependent surface charge $\sigma(\rho_b)$ due to a salt-concentration-dependent surface reaction.[50,51]

For nonvanishing applied potential drops ($\Delta\psi \neq 0$) not only an electric current $I = 2\pi\hat{\mathbf{x}}\cdot\int_0^R \mathbf{j}_e r \, dr$ (with $\hat{\mathbf{x}}$ the unit vector along the x-direction) and electro-osmotic flow $Q = 2\pi\hat{\mathbf{x}}\cdot\int_0^R \mathbf{u}(r) r \, dr$ are driven through the pore but also a salt current $J = 2\pi\hat{\mathbf{x}}\cdot\int_0^R \mathbf{j}_s(r) r \, dr$ where the bulk-excess salt current is primarily a conductive current through the EDL. In steady state this salt current must be laterally constant to prevent the buildup of salt through the pore, $\pi R^2(x)\,\partial_x\overline{\rho}_s = -\partial_x J = 0$, where $\overline{\cdots} = 2\pi(\pi R^2(x))^{-1}\int_0^{R(x)}\cdots r \, dr$ denotes the cross-sectional average of the salt concentration. The condition of a divergence-free flux (eq 6), which is necessary for a steady-state solution, leads to a differential equation for the cross-sectionally averaged salt concentration for $x \in \{0, L\}$

https://doi.org/10.1021/acsami.2c11467
ACS Appl. Mater. Interfaces 2022, 14, 56226−56236

$$D\partial_x\left(\pi R^2\partial_x\overline{\rho}_s + 2\pi R\sigma\frac{e\partial_x\psi}{k_BT}\right) - Q\partial_x\overline{\rho}_s = 0 \tag{7}$$

with the electric field $-\partial_x\psi = (\Delta\psi_p/L)R_bR_t/R^2(x)$[25] and the electro-osmotic flow in a conical channel $Q = -\Delta\psi_p(\pi R_tR_b/L)(\varepsilon\psi_0/\eta)$ (as derived beneath eq 2 in ref 25). In eq 7 the first term represents diffusion of salt through the bulk of the pore, the second term conduction of salt through the EDL, and the third term advection of salt through the bulk of the pore. In a cylinder with constant radius R this differential equation reduces to $D\partial_x^2\overline{\rho}_s - Q\partial_x\overline{\rho}_s = 0$, which with boundary conditions $\overline{\rho}_s(0) = \overline{\rho}_s(L) = 2\rho_b$ has the trivial solution of $\overline{\rho}_s = 2\rho_b$. Thus, for straight pores no current rectification is expected. For a conical geometry, the laterally changing radius $R(x)$ causes lateral variation of conductive currents $D\partial_x(2\pi R(x)\sigma e\partial_x\psi(x)/k_BT) \neq 0$, which frustrates the formation of a constant J and acts as a nonzero source term. For a negative surface charge, as is typically the case for silica, this source term is negative for $\Delta\psi > 0$, and thus the salt concentration in the pore decreases. For $\Delta\psi < 0$ this source term is positive, and thus the salt concentration increases. Solving for the cross-sectional average concentration profile $\overline{\rho}_s(x)$ leads to a nontrivial solution[25]

$$\overline{\rho}_s(x) - 2\rho_b = \frac{\Delta\rho}{\mathrm{Pe}}\left[\frac{x}{L}\frac{R_t}{R(x)} - \frac{\exp\left(\frac{x}{L}\frac{R_t^2}{R_bR(x)}\mathrm{Pe}\right) - 1}{\exp\left(\frac{R_t}{R_b}\mathrm{Pe}\right) - 1}\right] \tag{8a}$$

$$= \frac{\Delta\rho}{2|\mathrm{Pe}|}\left(\frac{R_b}{R(x)}\left(1 - \frac{x}{L}\left(1 + \frac{R_t}{R_b}\right)\right) \mp 1\right) \text{ if } \pm\mathrm{Pe} \gg \left(\frac{R_b}{R_t}\right)^2 \tag{8b}$$

where the tip Péclet number $\mathrm{Pe} \equiv -\Delta\psi_p(R_b/R_t)(\varepsilon\psi_0/D\eta)$ and $\Delta\rho \equiv 4(e\Delta\psi_p/k_BT)\mathrm{Du}(R_b/R_t - 1)\rho_b$ is a measure for the concentration polarization, with tip Dukhin number $\mathrm{Du} = \sigma/(2\rho_bR_t)$. Note that both Pe and Du carry a sign and the diode polarity stems from the sign of the Dukhin number.

Having obtained the salt concentration $\overline{\rho}_s(x)$ in eq 8 the resulting pore conductance $G(\Delta\psi) = I(\Delta\psi)/\Delta\psi$ is calculated by cross-sectionally integrating eq 2, which results in

$$G(\Delta\psi) = G_b(\Delta\psi)\left(1 + \frac{4\langle\lambda_D\rangle}{R_b + R_t}\left(\cosh\left(\frac{e\psi_0}{2k_BT}\right) - 1\right)\right) \tag{9}$$

Here $\langle\ldots\rangle = L^{-1}\int_0^L\ldots dx$ denotes the lateral average, and the bulk channel conductance is given by $G_b(\Delta\psi) = 4\langle\overline{\rho}_s\rangle R_tR_b(e^2D/k_BT)/(4L/\pi + R_b + R_t)$. This bulk conductance also accounts for the inlet and outlet resistance by incorporation of eq 1 and depends on $\Delta\psi$ through the potential dependence of $\langle\overline{\rho}_s\rangle$, which is obtained by numerical integration of eq 8. We note that eq 9 obtained from the PNPS eqs 2−6 has precisely the form expected from the circuit depicted in Figure 2a: it consists of the sum of a bulk and surface (pore) conductance, $G = G_b + G_s$ (Figure 2a, green), whereas the tip and base conductances (Figure 2a, red) stand in series with the pore and lower the total conductance per eq 1. The surface conductance $G_s = 4G_b\langle\lambda_D\rangle/(R_b + R_t)(\cosh(e\psi_0)/(2k_BT) - 1)$ will vary with concentration through the dependence of the "channel-weighted" Debye length $\langle\lambda_D\rangle \simeq (4\pi\lambda_B\langle\overline{\rho}_s\rangle)^{-1/2}$. In principle, we could include the advective (streaming current) contribution to eq 9, but its contribution to the surface conductance is proportional to $k_BT/(4\pi\eta\lambda_BD(\cosh(e\psi_0/2k_BT) - 1)) \ll 10^{-2}$ for all our parameter sets and hence can be neglected.[52]

It is important to note that while the advective contribution to the electric current I can be neglected, the advective contribution to the salt current J (eq 7) is key to current rectification as for ICR the flow rate determines the characteristic voltage $\Delta\psi_c$, known as the knee voltage for diodes. When $\Delta\psi_c \gg |\Delta\psi|$, the conductance is Ohmic (G_0), while for $\pm\Delta\psi \gg \Delta\psi_c$ the limiting diode conductance ($G_\pm$) has been reached. From eq 8 it can be seen that for large flow $|\mathrm{Pe}| \gg (R_b/R_t)^2$ the concentration profile $\overline{\rho}_s(x) - 2\rho_b \propto \Delta\rho/|\mathrm{Pe}|$ is potential-independent, and hence per eq 9 this limiting conductance $G_\pm$ has been reached. Hence, the characteristic potential $\Delta\psi_c$ is set by the potential for which $\mathrm{Pe} = (R_b/R_t)^2$, yielding

$$\frac{e\Delta\psi_c}{k_BT} = w(R_b/R_t)[1 + (\pi/4L)(R_b + R_t)] \tag{10}$$

where $w = eD\eta/(k_BT\varepsilon|\psi_0|)$ is the (dimensionless) ratio of the ionic to electro-osmotic mobility that quantifies the competition between the rate by which conduction adds ions to the concentration profile $\overline{\rho}_s(x)$ and electro-osmotic flow removes them. Note that this ratio depends only on electrolyte properties and surface potential, and it is not influenced by the geometry whatsoever, being constant ($w \simeq 0.3$) over all our geometries and concentrations. The term in the square brackets of eq 10 accounts for edge resistance and can be set to unity in the long-channel limit. While eq 9 can be used to describe the conductance for arbitrary $\Delta\psi$ by straightforward numerical integration of eq 8a, a more convenient closed form for the limiting conductances $G_\pm$ can be found when neglecting the second (surface) term for the electric conductance $G(\Delta\psi)$ (eq 9). This approximation therefore neglects surface conductance entirely and subsequently integrating eq 8b yields

$$\frac{G_{\pm,b}}{G_{0,b}} = 1 + 2w\mathrm{Du}\left[\frac{\log(R_b/R_t)}{R_b/R_t - 1} - \left(\frac{R_t}{R_b}\right)^{(1\pm1)/2}\right] \tag{11}$$

As such, current rectification is defined by the ratio $G_-/G_+ = \mathrm{ICR}$ where, as before, $\mathrm{Du} = \sigma/(2\rho_bR_t)$ represents the ratio of salt transport in the EDL with respect to salt transport in the bulk. The bracketed term of eq 11 fully captures the effect of geometry on the concentration profile $\overline{\rho}_s(x)$. This last term is zero for $R_t = R_b$, positive for G_+, and negative for G_- and reflects the influence of geometry on diode polarity. Equation 11 also straightforwardly gives a simple and convenient analytic expression for the ICR = G_-/G_+.

In the following sections we consider the small and large potential limits of eq 9 to interpret our experimental data by first considering the measured (Ohmic) conductance G_0 at small potential drops $|\Delta\psi| < \Delta\psi_c$ and then to describe ICR, which is given by the ratio of conductances G_-/G_+ in the limit of large positive (+) or negative (−) potential drops for $\pm\Delta\psi \gg \Delta\psi_c$.

OHMIC CONDUCTANCE

First we consider the Ohmic conductance, G_0, which is found at small potential drops $|\Delta\psi| < \Delta\psi_c$. In this case the laterally averaged concentration equals the bulk concentration $\langle\overline{\rho}_s\rangle = 2\rho_b$. Hence, G_0 is given by eq 9 where the bulk Ohmic conductance $G_{0,b} = 8R_tR_b(e^2D/k_BT)/(4L/\pi + R_b + R_t)\rho_b$, and the surface Ohmic conductance $G_{0,s}$ is determined by the equilibrium Debye length $\lambda_D = (8\pi\lambda_B\rho_b)^{-1/2}$. In this regime we find that eq 9 reduces to several well-known results depending on the geometry. The conductance of a long conical channel with negligible surface conductance is retrieved when $L \gg R_b > R_t \gg \lambda_D$,[25] the Hall conductance of a thin cylindrical pore with negligible surface conductance is retrieved when $L \simeq R_b = R_t \gg \lambda_D$,[39] and the conductance of a long cylindrical channel[52] is obtained when $L \gg R_b = R_t > \lambda_D$. Hence, eq 9 extends these classical results to short pores with unequal tip and base radii. Figure 3 shows the experimental Ohmic conductance obtained as $G_0 = (I(0.05\ \mathrm{V}) - I(-0.05\ \mathrm{V}))/0.1\ \mathrm{V}$ together with our theoretical model eq 9 for all four channels T1, T2, S1, and S2, where we use $\psi_0 = -0.21$ V as it provides the closest match to the data for all concentrations and geometries. Note that the classical long-channel theory that neglects entrance resistance through eq 1 would overestimate the conductance by a factor of about 2 for our parameters, as the effective potential drop is nearly halved ($0.46 < \Delta\psi_p/\Delta\psi < 0.68$) in our experimental geometries. This reduction of the effective potential drop highlights the importance of edge resistances.

https://doi.org/10.1021/acsami.2c11467
ACS Appl. Mater. Interfaces 2022, 14, 56226−56236

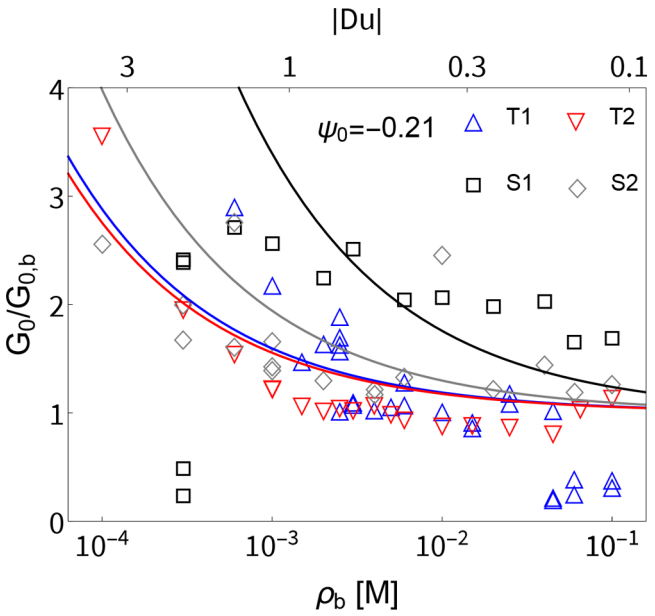

Figure 3. Ohmic conductance G_0 in units of the bulk conductance $G_{0,b}$ as a function of the bulk concentration ρ_b (lower axis) and Dukhin number $Du = \sigma/(2\rho_b R_t)$ (upper axis) with tip radius $R_t = 0.5$ μm representative for the tapered pores T1 and T2 and straight pores S1, but not for the straight pore S2 with radius $R_t = 1.5$ μm. The symbols denote the experimental measurements, and the lines with corresponding colors are plotted using eq 9 with a large surface potential $\psi_0 = -0.21$ V (see text). As expected, the conductance converges to the bulk conductance at high concentration while it increases to triple the bulk conductance at low concentrations due to the contribution of surface conductance.

It should be emphasized that the experimental conductance in Figure 3 is normalized by the theoretical bulk conductance $G_{0,b}$ from eq 9, which is determined by both pore geometry and electrolyte properties. At high concentrations this representation highlights that the surface conductance is negligible, as the conductance in units of $G_{0,b}$ approaches unity and the experimental data for different geometries collapse into a single curve. Note that eq 9 properly accounts for the inlet and outlet resistance at the highest concentration. Some of the deviation between experimental data and theory is attributed to morphological changes due to clogging over the course of the experiments (see, for instance, the SEM image of T1 after the experiments in SI-5).

At low concentrations, $\rho_b < 1$ mM, both the theoretical and experimental conductance rapidly increase as the concentration decreases, which is due to the surface conductance $G_{0,s}$ contribution increasing with the increasing Debye screening length. We observe that the concentration at which surface conductance becomes comparable to bulk conductance occurs when the tip Dukhin number approaches unity, $G_{0,s}/G_{0,b} \propto Du = \sigma/(2\rho_b R_t) \simeq 1$, which for both T1 and T2 occurs near $\rho_b \simeq 2$ mM for $\psi_0 = -0.21$ V. The experimental variation of conductance with concentration roughly scales as the inverse square of the concentration, increasing by a factor of 3 when the concentration is decreased by a factor of 10. This scaling can only be understood by using a concentration-independent ψ_0 as opposed to a concentration-independent surface charge density σ. With constant σ the Dukhin number scales as $Du \propto \rho_b^{-1}$ and introduces a surface conductance which varies by orders of magnitude in our concentration range, which is not observed. Instead, when using a constant ψ_0, the surface charge scales as $\sigma \propto 1/\lambda_D$ according to the Gouy−Chapman equation, in which case the proper scaling $Du \propto \rho_b^{-1/2}$ is immediately obtained. The existence of a constant surface potential implies that a chemical reaction is responsible for the surface charge varying with salt concentration. However, while Figure 3 indeed shows that the experimental conductance qualitatively follows the inverse square-root scaling, there is a minor quantitative deviation. We attribute this chiefly to charge regulation beyond the constant-potential model of the silica−water interface,[53] which could introduce variations in ψ_0 by a factor of ∼3 in the range 10^{-1}−10^{-4} M for silica.[50,51,54] We have not included this concentration effect as there is no

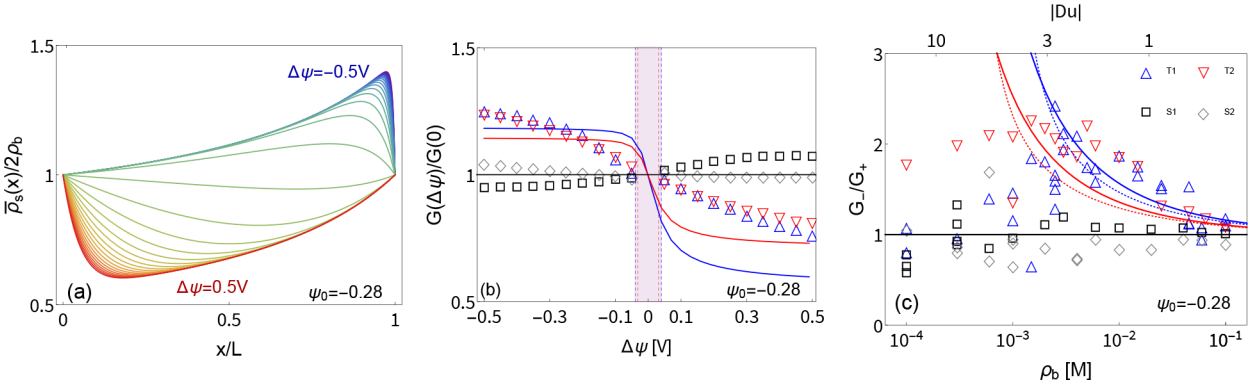

Figure 4. (a) Concentration profiles $\bar{\rho}_s(x)/2\rho_b$ for geometry T1 (see text) at a bulk concentration $\rho_b = 6$ mM as calculated by eq 8 for $\Delta\psi$ between −0.5 and 0.5 V with a step size of 0.03 V. Depletion occurs for positive potentials (red) while concentration increases at negative potentials (blue). (b) Conductance normalized by the conductance at $\Delta\psi = 0$ at varying potentials and the same concentration as in (a) where the different symbols represent the tapered (T1, T2) and straight (S1, S2) channels, and lines are plotted using the combination of eq 9 and eq 8a both with a surface potential of $\psi_0 = -0.28$ V. Vertical lines demarcating the shaded area are placed at the characteristic voltage $\Delta\psi_c \simeq \pm 0.05$ V with color corresponding to the respective geometry. Most variation of the experimental conductance occurs within the shaded region, after which the conductance converges to the limiting conductances $G_\pm$. (c) Current rectification given by the ratio G_-/G_+ which for experiments is taken as $G(\pm 0.5$ V) with varying concentration (lower axis) and Dukhin number for $R_t = 0.5$ μm (upper axis). Solid lines are plotted with our approximation eq 11 which neglects surface conductance, and dotted lines are from the full solution using the combination of eq 9 and eq 8a both using $\psi_0 = -0.28$ V. Peak experimental current rectification is reached near $Du \simeq 3$ while solid lines grow monotonically with Du.

https://doi.org/10.1021/acsami.2c11467
ACS Appl. Mater. Interfaces 2022, 14, 56226−56236

unanimous quantitative measurement of charge regulation for silica[50,51,53−55] and as to prevent overfitting.

■ ION CURRENT RECTIFICATION

We now turn to large potential drops where $|\Delta\psi| \gg \Delta\psi_c$ (eq 10) where we observe significant current rectification for tapered pores T1 and T2 and the conductance has converged to its limiting value $G_\pm$ (eq 11). Current rectification in conical pores is well established to be due to the salt concentration in the pore changing with the applied potential[25,56−58] as described in the Theoretical section. The dependence of the laterally averaged salt concentration $\langle\bar{\rho}_s\rangle$ on $\Delta\psi$ as in eq 8 in conjunction with our expression for the conductance (eq 9) immediately results in a voltage-dependent conductance. In Figure 4a we use eq 8 to plot the salt concentration profiles $\bar{\rho}_s(x)/(2\rho_b)$ in the conical pore T1 for $\Delta\psi$ between −0.5 and 0.5 V and a concentration ρ_b = 6 mM. It can be seen that for negative voltages there is a buildup of ions, while for positive voltage drops the pore becomes depleted. This increase and decrease, characteristic of the conical geometry, is highly dependent on the applied voltage but converges to a limiting concentration profile for which inhomogeneous conduction is balanced by advection. These limiting concentration profiles can deviate up to 50% from the bulk concentration and in turn significantly modulate the voltage-dependent conductance as can be seen in Figure 4b. Here we compare $G(\Delta\psi)$ from eq 9 with the experimental conductance normalized by the experimental Ohmic conductance $G(\Delta\psi = 0)$. We observe two plateaus of high and low conductance for the theoretical curves at large negative and positive voltages for the tapered pores. The transition between the two regimes occurs at the borders of the shaded region $|\Delta\psi| \leq \Delta\psi_c \simeq 0.05$ V, beyond which the conductance quickly converges to the limiting conductance $G_\pm$. In SI-7 we show more plots at different concentrations for comparison, which all show the same typical S-shaped curve with the exception for curves at ρ_b < 1 mM for which the experimental variation is larger due to leakage currents as discussed in the Experimental Section.

In Figure 4c we plot the experimental ICR against concentration and tip Dukhin number, together with results based on both eq 11 (solid) and the combination of eq 9 with eq 8a (dashed) using a fitted surface potential $\psi_0 = -0.28$ V in both cases. Theoretical and experimental ICR obey the same inverse square root scaling $G_-/G_+ \propto \rho_b^{-1/2}$ as was also observed for Ohmic conductance, which is again due to the concentration dependence of Du at fixed surface potential ψ_0. Interestingly, we find that eq 11 is a good approximation for the combination of eq 9 with eq 8a. The unexpected quality of our approximation eq 11 is a result of a cancellation of errors: an increase of Ohmic conduction due to surface conductance decreases ICR while the variation of surface conductance with concentration polarization increases ICR.

At low concentrations the inverse square root dependence of ICR breaks down around $\rho_b \simeq 2$ mM, where the experimental ICR peaks while our theory predicts that ICR should keep increasing with decreasing concentration. Such a peak in ICR has been previously observed in long microchannels[29,33,56] and assigned to the emergence of EDL overlapping at low concentrations. Here the concentration depletion in the pore only allows for minor EDL overlap at the tip, as the screening length is at least an order of magnitude smaller than the tip size in our experiments. Other theoretical works predict a peak in ICR at 1 < Du < 10,[26,30] which is attributed to salt transport in the EDL dominating the total salt transport, an effect that is not captured in our model. In SI-9 we plot the pore selectivity as defined in ref 30 for our tapered geometries with $\psi_0 = -0.21$ V and find a maximum near ρ_b = 2 mM, in line with our experiments.

■ DISCUSSION OF THE LARGE SURFACE POTENTIAL

Both conductance G_0 and current rectification G_-/G_+ are visually fitted using ψ_0 as the only fit parameter which we keep constant for all geometries and concentrations, yielding $\psi_0 = -0.21$ V for G_0 and $\psi_0 = -0.28$ V for G_-/G_+. However, the surface chemistry of the silica interface is well studied, and a much lower surface potential between −0.03 V and −0.1 V is expected in our experimental conditions.[55] While surface potentials may vary quite significantly between different measurement methods, protocols and even subsequent measurements,[55] a discrepancy that exceeds 0.1 V is excessive. From the Gouy−Chapman equation we find that a pore with a surface potential between −0.21 and −0.28 V would contain approximately 15−60 times more charge than for a typical literature surface potential of −0.07 V. Such a large discrepancy cannot be explained by subtle experimental factors. Induced charge due to membrane capacitance may partly explain the large apparent charge at large applied potentials ($\Delta\psi$).[59] However, previous work found that induced charge on 55 nm thick silicon membranes is comparable to the surface charge of silica.[60] As the membrane capacitance and therefore the induced charge scales with the inverse of membrane thickness, we expect the (material specific) influence of induced charge to be minor in the 2 μm thick membranes used here. Furthermore, the large apparent charge required to explain Ohmic conductance at $\Delta\psi \sim 0$, can not be justified by induced charge. We therefore assume that this deviation stems from our theoretical model not including all of the key physics.

In our analysis we exclude the charge on the planar membrane outside the pore, effectively neglecting an edge EDL conductance G_s^{base} and G_s^{tip} as depicted in Figure 2a. Other authors have noted that this region on the outside of the pore can contribute to both the Ohmic conductance[38,40] and the current rectification[41,42] for thin pores with $R_b/L \leq 1$. The charge on the outside of the membrane not only increases the edge conductance as noted by[2,38] but surprisingly can also induce excess ICR.[41] This excess ICR is due to a radial electric field driving an inhomogeneous salt current through the EDL ouside of the pore, leading to accumulation/depletion of salt in the reservoir as we demonstrate in SI-6. While excess ICR and excess conductance both occur in the EDL outside of the pore, they are distinct phenomena whose scaling and characteristic length scales may differ qualitatively, explaining why our experimental G_0 and G_+/G_- are better accounted for with two different surface potentials, $\psi_0 = -0.21$ V and $\psi_0 = -0.28$ V, respectively.

Considering that the charge on the outside of the membrane can contribute to both ICR and increased conductance, we suggest to assign the excess charge from the large, fitted, surface potential ψ_0 to the charge located on the planar membrane outside of the pore. We estimate this charged-surface area A_{out} outside the pore as $A_{out} = A_{pore}((\sigma_{app}/\sigma_{lit}) - 1)$, where A_{out} is the (circular) area outside of the pore contributing to entrance-surface conductance, A_{pore} is the surface area of the conical pore, $\sigma_{app} = \sinh(\psi_0 e/2k_BT)/(2\pi\lambda_B\lambda_D)$ is the apparent (Gouy−Chapman) surface charge

https://doi.org/10.1021/acsami.2c11467
ACS Appl. Mater. Interfaces 2022, 14, 56226−56236

density resulting from the fitted surface potential (with ψ_0 = −0.21 V for Ohmic conductance and ψ_0 = −0.28 V for ICR), and σ_{lit} = $\sinh(-0.07V(e/2k_BT))/(2\pi\lambda_B\lambda_D)$ is the surface charge density as calculated from a literature surface potential of −0.07 V. With these values we find that the outer-membrane EDL within a radius of about 15.0 μm from the pore center contributes to ICR, while a shorter radius of only 7.4 μm contributes to Ohmic conductance. This latter value closely corresponds to the Dukhin length $\sigma/(2\rho_b) \simeq 7$ μm at 10^{-4} M, which was predicted by refs 2 and 38 to set the length scale for (Ohmic) outer-membrane surface conductance.

To verify this larger surface contribution of 15 μm for ICR, we derive a solution for the concentration polarization far from the pore in SI-6 and find that the concentration profile in the bulk obeys a long-ranged inverse square law decay $\rho_s(x,r) \propto (r^2 + x^2)^{-1}$ like the electric field with a prefactor proportional to the inverse aspect ratio R_b/L. This prefactor indicates that outer-membrane concentration polarization only occurs for short pores, while the inverse square decay indicates that the concentration profile decays over lengths much larger than the radius. Both these observations support the hypothesis that surface charge far from the pore can contribute to current rectification for low-aspect ratio pores. Unfortunately, we were unable to construct a theory simultaneously accounting for concentration polarization inside and outside the pore, while numerical (COMSOL) calculations of the full PNPS (eqs 2−6) proved unstable. To experimentally test our hypothesis, we construct a 5 × 5 array of conical pores with dimensions $R_t \simeq 0.35$ μm, $R_b \simeq 1.4$ μm, and $L \simeq 2$ μm with a spacing of 10 μm between the pore centers ($\approx 10^6$ pores/cm^2). In Figure 5a we show the ICR calculated with eq 11 using the literature surface potential ψ_0 = −0.07 V (dashed line) and the large surface potential obtained from the single pore fitted with ψ_0 = −0.28 V (solid line) together with the experimental data for the array (symbols). We observe that ICR is greatly reduced for the array, virtually disappearing over the whole concentration range. In contrast, the Ohmic conductance of the array is essentially 25 times the single pore conductance given by eq 9 as shown in Figure 5b. Considering that the single pore results are based on the fitted value of ψ_0 = −0.21 V, the surface conductance therefore remains excessively large compared to the expectation at a literature surface potential of ψ_0 = −0.07 V (solid line). In line with our hypothesis, these observations therefore surprisingly imply that the charge on the outside of the membrane contributes over a smaller range to conductance than to ICR, so that interference only occurs for the latter at this spacing.

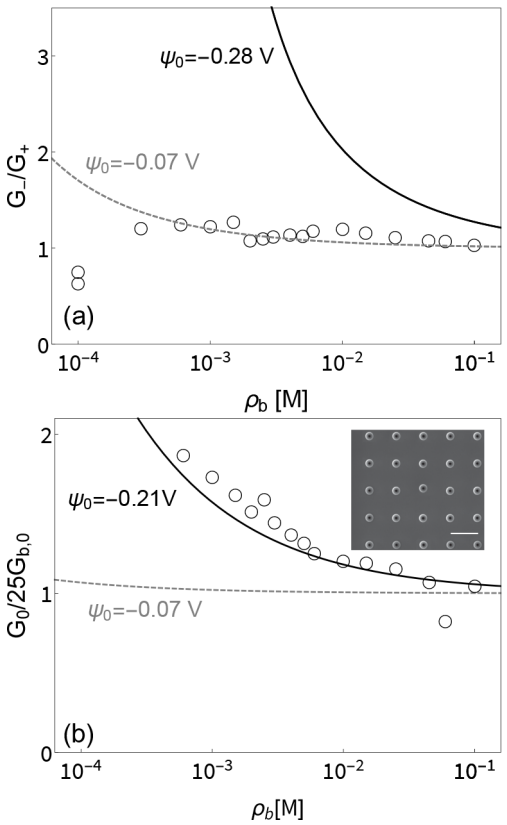

Figure 5. (a) Current rectification G_-/G_+ as a function of concentration (lower axis) for an array of 25 pores. The symbols denote the experimental measurements, and the lines are plotted using eq 11 using a surface potential of ψ_0 = −0.28 V (black, continuous) and ψ_0 = −0.07 V (gray, dashed). No current rectification is found in the experiment, in line with a pore with a surface potential of ψ_0 = −0.07 V. (b) Dimensionless Ohmic conductance G_0 in units of the bulk conductance $G_{0,b}$ in the same representation as in Figure 3 with lines plotted using eq 9. The measured conductance corresponds essentially to 25 times the conductance of a single pore with ψ_0 = −0.21 V. The inset of (b) shows an SEM image of the array directly after fabrication; the scale bar is 10 μm.

CONCLUSION

To summarize, we have presented experimental and theoretical results on ion current rectification (ICR) in tapered micropores connecting aqueous KCl solutions, leading to three main results.

(i) We demonstrate the existence of ICR in conical micropores fabricated in crystalline silicon membranes without further chemical modification at KCl concentrations where the (bulk) electrolyte screening length is much smaller than the pore size and which is absent in straight cylindrical pores.

(ii) We derive an expression for the conductance of short conical pores accounting for both the EDL within the channel as well as the edge resistance at the tip and base of the pore. These edge resistances approximately halve the Ohmic conductance in our experimental geometries. Our expression (eq 9) reverts to the Hall conductance in the case of thin cylindric pores,[39] conical conductance in the case of long cones,[25] and the well-known conductance of straight cylinders with EDL's for large aspect ratio channels.[52] We find an expression for the characteristic voltage at which current rectification occurs, $\Delta\psi_c \simeq 0.05$ V in our geometries, and find a new closed-form expression (eq 11) for the limiting ICR at large potential drops. While, like other authors, we find that rectification scales with the Dukhin number, our expression contains two new dimensionless terms: the ratio w of the ionic and electro-osmotic (fluid) mobility and a term describing the influence on geometry which solely depends on the tip-to-base ratio. Using two different surface potentials (ψ_0 = −0.21 V for Ohmic conductance and ψ_0 = −0.28 V), our theory closely matches our experimental results for all but the lowest concentrations and largest potential drops. In this regime of extreme depletion minor EDL overlap occurs at the tip, invalidating the starting assumption of nonoverlapping EDL's in our theory.

(iii) Finally, we discuss the physical interpretation of the surface potential ψ_0 which is our sole fit parameter. Our fitted

https://doi.org/10.1021/acsami.2c11467
ACS Appl. Mater. Interfaces 2022, 14, 56226−56236

surface potential is excessively large compared to literature values and should not be interpreted as the actual potential but rather as an apparent surface potential. This apparent potential is inflated by the contribution of charge on the outside of the membrane, a region explicitly excluded from our theoretical description. We estimate from the fitted ψ_0 that charge on the membrane surface within about 7.4 μm of the pore contributes to (Ohmic) conductance at low potentials and within 15.0 μm to ICR at larger potentials. We test this hypothesis by fabricating an array of 25 pores with a 10 μm separation of the pore centers ($\approx 10^6$ pores/cm^2) with no overlap of the low potential (Ohmic) interaction length and large overlap of the high potential (ICR) interaction length. While we observe no pore−pore interference for Ohmic conduction at low potentials, we indeed find that ICR vanishes in the array, in agreement with our hypothesis. The interaction length for Ohmic conduction is known to be set by the Dukhin length[2,38] while for ICR we show that a long-ranged, inverse-square-distance decay determines the pore−pore interaction, in line with our experimental observations. For thin membranes this apparent contribution of the charge on the outside of the membrane to both surface conductance and ICR may be beneficial for single pores; however, these contributions could be detrimental in densely packed arrays that would be desirable for applications. Further investigation of the interaction length for outer-membrane conductance and ICR with different pore densities is therefore particularly relevant. Here, the presented crystalline silicon membranes provide an attractive platform compatible with conventional fabrication methods for e.g. creating homogeneous pore walls through wet etching or engineering of the pore behavior by modification of the outer-membrane surface.

METHODS

Pore Fabrication. Crystalline silicon membranes were purchased from Norcada (SM5200N, thickness 2 ± 0.5 μm). Pores were milled in the membrane with a focused ion beam (FEI Helios Nanolab 600, Ga ions), with tapered pores created by milling concentric circles. Scanning electron miscroscopy images were made in the same system.

Current Measurements. $I-V$ measurements were conducted in a homemade cell consisting of two reservoirs, with the membrane fixed in between (as shown in SI-2). The reservoirs are filled with aqueous solutions with equal concentration of KCl (99.99% from Sigma-Aldrich, in Milli-Q ultrapure water). Measurements are done using a Ag/AgCl wire electrode in each reservoir, connected to a potentiostat (CH760E) in a two-electrode configuration with the working electrode facing the large opening (base) for the tapered channels. Quasi-static $I-V$ curves were recorded using staircase voltammetry from −1 to 1 V and back, with potential steps of 0.05 V and with the system set to rest for 150 s at −1 V before starting the measurement. Each potential is maintained for a period of 10 s, with the current recorded for the last 0.5 s. Data shown in Figure 1 are obtained from averaging 1−4 cycles.

Electrode Preparation. Ag/AgCl wires were fabricated following the protocol in ref 61 by immersing Ag wires (0.35 mm diameter, 99.99%) in 0.1 M nitric acid to remove the native oxide and then rinsed with ultrapure water. The cleaned wire was using as a working electrode in a three-electrode setup with a platinum counter and quasi-reference electrode in an aqueous solution of 3 M KCl. The Ag wire was coated with AgCl by applying 2 V vs the Pt wire QRE for 10 min.

ASSOCIATED CONTENT

Supporting Information

The Supporting Information is available free of charge at https://pubs.acs.org/doi/10.1021/acsami.2c11467.

Figures S1−S9 (PDF)

AUTHOR INFORMATION

Corresponding Author

Esther Alarcon-Llado − *Center for Nanophotonics, AMOLF, 1098 XG Amsterdam, Netherlands;* orcid.org/0000-0001-7317-9863; Email: e.alarconllado@amolf.nl

Authors

Mark Aarts − *Center for Nanophotonics, AMOLF, 1098 XG Amsterdam, Netherlands*

Willem Q. Boon − *Institute for Theoretical Physics, Utrecht University, 3584 CC Utrecht, Netherlands;* orcid.org/0000-0003-3385-1904

Blaise Cuénod − *Center for Nanophotonics, AMOLF, 1098 XG Amsterdam, Netherlands*

Marjolein Dijkstra − *Soft Condensed Matter, Debye Institute for Nanomaterials Science, Utrecht University, 3584 CC Utrecht, Netherlands;* orcid.org/0000-0002-9166-6478

René van Roij − *Institute for Theoretical Physics, Utrecht University, 3584 CC Utrecht, Netherlands*

Complete contact information is available at: https://pubs.acs.org/10.1021/acsami.2c11467

Author Contributions

M.A. and W.Q.B. contributed equally to this work.

Notes

The authors declare no competing financial interest.

ACKNOWLEDGMENTS

This work is part of the research program at The Netherlands Organisation for Scientific Research (NWO). We acknowledge R. Brakkee and D. Ursem for contributions to the project and D. Koletzki for fabrication of the setup. This work is part of the D-ITP consortium, a program of The Netherlands Organisation for Scientific Research (NWO) that is funded by the Dutch Ministry of Education, Culture and Science (OCW).

REFERENCES

(1) Critical Knowledge Gaps in Mass Transport through Single-Digit Nanopores: A Review and Perspective. *J. Phys. Chem. C* **2019**, *123*, 21309−21326.

(2) Bocquet, L. Nanofluidics coming of age. *Nat. Mater.* **2020**, *19*, 254−256.

(3) Nishizawa, M.; Menon, V. P.; Martin, C. R. Metal Nanotubule Membranes with Electrochemically Switchable Ion-Transport Selectivity. *Science* **1995**, *268*, 700−702.

(4) Vlassiouk, I.; Smirnov, S.; Siwy, Z. Ionic Selectivity of Single Nanochannels. *Nano Lett.* **2008**, *8*, 1978−1985.

(5) Daiguji, H.; Oka, Y.; Shirono, K. Nanofluidic Diode and Bipolar Transistor. *Nano Lett.* **2005**, *5*, 2274−2280.

(6) Kalman, E. B.; Vlassiouk, I.; Siwy, Z. S. Nanofluidic Bipolar Transistors. *Adv. Mater.* **2008**, *20*, 293−297.

(7) Rees, H. R.; Anderson, S. E.; Privman, E.; Bau, H. H.; Venton, B. J. Carbon Nanopipette Electrodes for Dopamine Detection in Drosophila. *Analytical chemistry* **2015**, *87*, 3849−3855.

(8) Wang, Y.; Wang, D.; Mirkin, M. V. *Physical and Engineering Sciences* **2017**, *473*, 20160931.

(9) Vlassiouk, I.; Kozel, T. R.; Siwy, Z. S. Biosensing with Nanofluidic Diodes. *J. Am. Chem. Soc.* **2009**, *131*, 8211−8220.
(10) Piruska, A.; Gong, M.; Sweedler, J. V.; Bohn, P. W. Nanofluidics in Chemical Analysis. *Chem. Soc. Rev.* **2010**, *39*, 1060−1072.
(11) Liu, Z.; Zhang, S.; Cheng, M.; Yang, L.; Li, G.; Xu, W.; Qu, H.; Liang, F.; Cheng, J.; Li, H. Highly Enantioselective Recognition of S-Ibuprofen by a Host-Guest Induced Chiral Nanochannel. *Analyst* **2022**, *147*, 1803−1807.
(12) van der Heyden, F. H. J.; Bonthuis, D. J.; Stein, D.; Meyer, C.; Dekker, C. Electrokinetic Energy Conversion Efficiency in Nanofluidic Channels. *Nano Lett.* **2006**, *6*, 2232−2237.
(13) Xiao, K.; Jiang, L.; Antonietti, M. Ion Transport in Nanofluidic Devices for Energy Harvesting. *Joule* **2019**, *3*, 2364−2380.
(14) Wang, D.; Kvetny, M.; Liu, J.; Brown, W.; Li, Y.; Wang, G. Transmembrane Potential Across Single Conical Nanopores and Resulting Memristive and Memcapacitive Ion Transport. *J. Am. Chem. Soc.* **2012**, *134*, 3651−3654.
(15) Wang, D.; Wang, G. Dynamics of Ion Transport and Electric Double Layer in Single Conical Nanopores. *J. Electroanal. Chem.* **2016**, *779*, 39−46.
(16) Han, S. H.; Oh, M.-A.; Chung, T. D. Iontronics: Aqueous Ion-Based Engineering for Bioinspired Functionalities and Applications. *Chemical Physics Reviews* **2022**, *3*, 031302.
(17) Siria, A.; Bocquet, M.-L.; Bocquet, L. New Avenues for the Large-Scale Harvesting of Blue Energy. *Nature Reviews Chemistry* **2017**, *1*, 0091.
(18) Hou, X.; Guo, W.; Jiang, L. Biomimetic Smart Nanopores and Nanochannels. *Chem. Soc. Rev.* **2011**, *40*, 2385−2401.
(19) Bush, S. N.; Volta, T. T.; Martin, C. R. Chemical Sensing and Chemoresponsive Pumping with Conical-Pore Polymeric Membranes. *Nanomaterials* **2020**, *10*, 571.
(20) Xiong, T.; Zhang, K.; Jiang, Y.; Yu, P.; Mao, L. Ion Current Rectification: from Nanoscale to Microscale. *Science China Chemistry* **2019**, *62*, 1346−1359.
(21) Woermann, D. Electrochemical Transport Properties of a Cone-Shaped Nanopore: High and Low Electrical Conductivity States Depending on the Sign of an Applied Electrical Potential Difference. *Phys. Chem. Chem. Phys.* **2003**, *5*, 1853−1858.
(22) Woermann, D. Electrochemical Transport Properties of a Cone-Shaped Nanopore: Revisited. *Phys. Chem. Chem. Phys.* **2004**, *6*, 3130−3132.
(23) Ghosal, S.; Sherwood, J. D.; Chang, H.-C. Solid-State Nanopore Hydrodynamics and Transport. *Biomicrofluidics* **2019**, *13*, 011301.
(24) Siwy, Z. S. Ion-Current Rectification in Nanopores and Nanotubes with Broken Symmetry. *Adv. Funct. Mater.* **2006**, *16*, 735−746.
(25) Boon, W. Q.; Veenstra, T. E.; Dijkstra, M.; van Roij, R. Pressure-Sensitive Ion Conduction in a Conical Channel: Optimal Pressure and Geometry. *Phys. Fluids* **2022**, *34*, 101701.
(26) Poggioli, A. R.; Siria, A.; Bocquet, L. Beyond the Tradeoff: Dynamic Selectivity in Ionic Transport and Current Rectification. *J. Phys. Chem. B* **2019**, *123*, 1171−1185.
(27) Cheng, L.-J.; Guo, L. J. Rectified Ion Transport through Concentration Gradient in Homogeneous Silica Nanochannels. *Nano Lett.* **2007**, *7*, 3165−3171.
(28) Graf, M.; Lihter, M.; Unuchek, D.; Sarathy, A.; Leburton, J.-P.; Kis, A.; Radenovic, A. Light-Enhanced Blue Energy Generation Using MoS2 Nanopores. *Joule* **2019**, *3*, 1549−1564.
(29) Vlassiouk, I.; Smirnov, S.; Siwy, Z. Nanofluidic Ionic Diodes. Comparison of Analytical and Numerical Solutions. *ACS Nano* **2008**, *2*, 1589−1602.
(30) Dal Cengio, S.; Pagonabarraga, I. Confinement-Controlled Rectification in a Geometric Nanofluidic diode. *J. Chem. Phys.* **2019**, *151*, 044707.
(31) Kovarik, M. L.; Zhou, K.; Jacobson, S. C. Effect of Conical Nanopore Diameter on Ion Current Rectification. *J. Phys. Chem. B* **2009**, *113*, 15960−15966.
(32) Lin, C.-y.; Yeh, L.-h.; Siwy, Z. S. Voltage-Induced Modulation of Ionic Concentrations and Ion Current Rectification in Mesopores with Highly Charged Pore Walls. *J. Phys. Chem. Lett.* **2018**, *9*, 393−398.
(33) Cervera, J.; Schiedt, B.; Neumann, R.; Mafé, S.; Ramírez, P. Ionic Conduction, Rectification, and Selectivity in Single Conical Nanopores. *J. Chem. Phys.* **2006**, *124*, 104706.
(34) Zhou, K.; Perry, J. M.; Jacobson, S. C. Transport and Sensing in Nanofluidic Devices. *Annual Review of Analytical Chemistry* **2011**, *4*, 321−341.
(35) Jubin, L.; Poggioli, A.; Siria, A.; Bocquet, L. Dramatic Pressure-Sensitive Ion Conduction in Conical Nanopores. *Proc. Natl. Acad. Sci. U. S. A.* **2018**, *115*, 4063−4068.
(36) Lin, C.-Y.; Combs, C.; Su, Y.-S.; Yeh, L.-H.; Siwy, Z. S. Rectification of Concentration Polarization in Mesopores Leads To High Conductance Ionic Diodes and High Performance Osmotic Power. *J. Am. Chem. Soc.* **2019**, *141*, 3691−3698.
(37) He, X.; Zhang, K.; Li, T.; Jiang, Y.; Yu, P.; Mao, L. Micrometer-Scale Ion Current Rectification at Polyelectrolyte Brush-Modified Micropipets. *J. Am. Chem. Soc.* **2017**, *139*, 1396−1399.
(38) Lee, C.; Joly, L.; Siria, A.; Biance, A.-L.; Fulcrand, R.; Bocquet, L. Large Apparent Electric Size of Solid-State Nanopores Due to Spatially Extended Surface Conduction. *Nano Lett.* **2012**, *12*, 4037−4044.
(39) Hall, J. E. Access Resistance of a Small Circular Pore. *J. Gen. Physiol.* **1975**, *66*, 531−532.
(40) Xiang, F.; Dong, M.; Liang, S.; Zhang, W.; Guan, W. Modeling Pyramidal Silicon Nanopores with Effective Ion Transport. *Nanotechnology* **2022**, *33*, 485503.
(41) Yossifon, G.; Mushenheim, P.; Chang, Y.-C.; Chang, H.-C. Eliminating the Limiting-Current Phenomenon by Geometric Field Focusing into Nanopores and Nanoslots. *Phys. Rev. E* **2010**, *81*, 046301.
(42) Ma, Y.; Guo, J.; Jia, L.; Xie, Y. Entrance Effects Induced Rectified Ionic Transport in a Nanopore/Channel. *ACS Sens.* **2018**, *3*, 167−173.
(43) Su, J.; Ji, D.; Tang, J.; Li, H.; Feng, Y.; Cao, L.; Jiang, L.; Guo, W. Anomalous Pore-Density Dependence in Nanofluidic Osmotic Power Generation. *Chin. J. Chem.* **2018**, *36*, 417−420.
(44) Kowalczyk, S. W.; Grosberg, A. Y.; Rabin, Y.; Dekker, C. Modeling the Conductance and DNA Blockade of Solid-State Nanopores. *Nanotechnology* **2011**, *22*, 315101.
(45) Kirby, B. J.*Micro-and Nanoscale Fluid Mechanics: Transport in Microfluidic Devices*; Cambridge University Press: 2010.
(46) Delgado, A. V.; González-Caballero, F.; Hunter, R.; Koopal, L. K.; Lyklema, J. Measurement and Interpretation of Electrokinetic Phenomena (IUPAC technical report). *Pure Appl. Chem.* **2005**, *77*, 1753−1805.
(47) Harned, H. S.; Nuttall, R. L. The Differential Diffusion Coefficient of Potassium Chloride in Aqueous Solutions. *J. Am. Chem. Soc.* **1949**, *71*, 1460−1463.
(48) *CRC Handbook of Chemistry and Physics*; CRC Press: 2004; Vol. *85*.
(49) Adamson, A. W.; Gast, A. P.*Physical Chemistry of Surfaces*; Interscience Publishers: New York, 1967; Vol. *150*.
(50) Szekeres, M.; Dékány, I.; De Keizer, A. Adsorption of Dodecyl Pyridinium Chloride on Monodisperse Porous Silica. *Colloids Surf., A* **1998**, *141*, 327−336.
(51) Janusz, W. The Structure of the Electrical Double Layer at the LiChrospher-Type Adsorbent/Aqueous Electrolyte Solution Interface. *Adsorption Science & Technology* **1996**, *14*, 151−161.
(52) Werkhoven, B. L.; van Roij, R. Coupled Water, Charge and Salt Transport in Heterogeneous Nano-Fluidic Systems. *Soft Matter* **2020**, *16*, 1527−1537.
(53) Zhao, C.; Ebeling, D.; Siretanu, I.; van den Ende, D.; Mugele, F. Extracting Local Surface Charges and Charge Regulation Behavior from Atomic Force Microscopy Measurements at Heterogeneous Solid-Electrolyte Interfaces. *Nanoscale* **2015**, *7*, 16298−16311.

https://doi.org/10.1021/acsami.2c11467
ACS Appl. Mater. Interfaces 2022, 14, 56226−56236

(54) Iler, R. K.*The Colloid Chemistry of Silica and Silicates*; LWW: 1955; Vol. *80*, p 666.
(55) Kosmulski, M.*Chemical Properties of Material Surfaces*; CRC Press: 2001; Vol. *102*.
(56) White, H. S.; Bund, A. Ion Current Rectification at Nanopores in Glass Membranes. *Langmuir* **2008**, *24*, 2212−2218.
(57) Wen, C.; Zeng, S.; Li, S.; Zhang, Z.; Zhang, S.-L. On Rectification of Ionic Current in Nanopores. *Analytical chemistry* **2019**, *91*, 14597−14604.
(58) Proctor, J. E. *Theory of Ion Transport and Ion Current Rectification in Nanofluidic Diodes* **2021**, 105.
(59) de Souza, J. P.; Chow, C.-M.; Karnik, R.; Bazant, M. Z. Nonlinear Ion Transport Mediated by Induced Charge in Ultrathin Nanoporous Membranes. *Phys. Rev. E* **2021**, *104*, 044802.
(60) Yao, Y.; Wen, C.; Pham, N. H.; Zhang, S.-L. On Induced Surface Charge in Solid-State Nanopores. *Langmuir* **2020**, *36*, 8874−8882.
(61) Inamdar, S. N.; Bhat, M. A.; Haram, S. K. Construction of Ag/AgCl Reference Electrode from Used Felt-Tipped Pen Barrel for Undergraduate Laboratory. *J. Chem. Educ.* **2009**, *86*, 355.

https://doi.org/10.1021/acsami.2c11467
ACS Appl. Mater. Interfaces 2022, 14, 56226−56236